Acta Crystallographica Section D
Biological Crystallography
ISSN 1399-0047

The family-wide structure and function of human dual-specificity protein phosphatases

Dae Gwin Jeong,[a]‡ Chun Hua Wei,[b]‡ Bonsu Ku,[a]‡ Tae Jin Jeon,[b] Pham Ngoc Chien,[b] Jae Kwan Kim,[c] So Ya Park,[b] Hyun Sook Hwang,[b] Sun Young Ryu,[b] Hwangseo Park,[d] Deok-Soo Kim,[c] Seung Jun Kim[a]* and Seong Eon Ryu[b]*

[a]Medical Proteomics Research Center, KRIBB, Daejeon, Republic of Korea, [b]Department of Bioengineering, College of Engineering, Hanyang University, Seoul, Republic of Korea, [c]Department of Industrial Engineering, College of Engineering, Hanyang University, Seoul, Republic of Korea, and [d]Department of Bioscience and Biotechnology, Sejong University, Seoul, Republic of Korea

‡ These authors contributed equally to this work.

Correspondence e-mail: ksj@kribb.re.kr, ryuse@hanyang.ac.kr

Received 20 May 2013
Accepted 31 October 2013

PDB references: DUSP8, 4jmk; DUSP11, 4jmj; DUSP12, 4ki9

Dual-specificity protein phosphatases (DUSPs), which dephosphorylate both phosphoserine/threonine and phosphotyrosine, play vital roles in immune activation, brain function and cell-growth signalling. A family-wide structural library of human DUSPs was constructed based on experimental structure determination supplemented with homology modelling. The catalytic domain of each individual DUSP has characteristic features in the active site and in surface-charge distribution, indicating substrate-interaction specificity. The active-site loop-to-strand switch occurs in a subtype-specific manner, indicating that the switch process is necessary for characteristic substrate interactions in the corresponding DUSPs. A comprehensive analysis of the activity–inhibition profile and active-site geometry of DUSPs revealed a novel role of the active-pocket structure in the substrate specificity of DUSPs. A structure-based analysis of redox responses indicated that the additional cysteine residues are important for the protection of enzyme activity. The family-wide structures of DUSPs form a basis for the understanding of phosphorylation-mediated signal transduction and the development of therapeutics.

1. Introduction

Protein tyrosine phosphatases (PTPs) dephosphorylate the proteins that are phosphorylated during cellular signalling and regulation (Tonks, 2006). PTP-mediated dephosphorylation regulates protein activities either negatively or positively and plays vital roles in various diseases, including cancers, vascular diseases, immune diseases and neurological diseases (Sawyer *et al.*, 2005). The human genome contains approximately 110 PTP members with common catalytic domains and significant sequence and structural homology (Alonso, Sasin *et al.*, 2004). Although the originally characterized PTPs only had dephosphorylating enzyme activities towards phosphotyrosine, there are a number of PTPs that dephosphorylate both phosphoserine/threonine and phosphotyrosine.

Mitogen-activated protein kinase phosphatases (MAPK phosphatases or MKPs), which are dual-specificity phosphatases, dephosphorylate the threonine-*X*-tyrosine (T*X*Y) motif of MAPKs (Boutros *et al.*, 2008). These molecules contain a MAPK-binding domain (MKB) at their N-termini and a phosphatase catalytic domain at their C-termini. By regulating the activity of MAPK signalling pathways, MKPs are pivotal players in cell growth and have been implicated in cell growth-related diseases (Boutros *et al.*, 2008; Jeffrey *et al.*, 2007). Atypical dual-specificity phosphatases (A-DUSPs) were identified based on their homology to the *Vaccina virus* H1 gene product (VH1; Guan *et al.*, 1991; Alonso, Burkhalter *et al.*, 2004; Koksal *et al.*, 2009; Patterson *et al.*, 2009). Although

Table 1
Structures of human DUSP catalytic domains.

Name	Alias	MKP†	PDB entry‡	ASC§	Ions¶	Oligomer††	References
DUSP1	MKP-1	MKB	Mod	1	—	—	This study‡‡
DUSP2	PAC-1	MKB	1m3g	2	—	—	Farooq *et al.* (2003)
DUSP3	VHR	Act	1vhr	1	S	—	Yuvaniyama *et al.* (1996)
DUSP4	MKP-2, hVH2	MKB	3ezz	1	S	24-mer	Jeong *et al.* (2009)‡‡
DUSP5	hVH3	MKB	2g6z	1	S	Dimer	Jeong *et al.* (2007)‡‡
DUSP6	MKP-3, Pyst1	MKB	1mkp	2	Cl	—	Stewart *et al.* (1999)
DUSP7	MKP-X, Pyst2	MKB	Mod	2	—	—	This study‡‡
DUSP8	hVH5, hVH8	MKB	Exp	1	S	—	This study‡‡
DUSP9	MKP-4, Pyst3	MKB	2hxp/3lj8	2	P/—	—	Almo *et al.* (2007)/Jeong *et al.* (2011)‡‡
DUSP10	MKP-5	MKB	1zzw/2oud	1	S/Cl	—	Jeong, Yoon *et al.* (2006)‡‡/Tao & Tong (2007)
DUSP11	PIR1	—	Exp	3	P, Cl	—	This study‡‡
DUSP12	HYVH1, GKAP	—	Exp	1	P	—	This study‡‡
DUSP13a	BEDP	—	Mod	3	—	Dimer	This study‡‡
DUSP13b	TMDP		2gwo/2pq5	1	—/—	—	Kim *et al.* (2007)‡‡/Structural Genomics Consortium (unpublished work)
DUSP14	MKP-6	Act	2wgp	1	P	—	Lountos *et al.* (2009)
DUSP15	VHY	Act	1yz4	1	S	—	Yoon *et al.* (2005)‡‡
DUSP16	MKP-7	MKB	Mod	1	—	—	This study‡‡
DUSP17	DUSP19	—	—	—	—	—	—
DUSP18	DUSP20	Act	2esb	1	A	—	Jeong, Cho *et al.* (2006)‡‡
DUSP19	SKRP1	Act	3s4e	1	P, S	—	Wei *et al.* (2011)‡‡
DUSP20	DUSP18	—	—	—	—	—	—
DUSP21	LMW-DUSP21	Cont	Mod	1	—	—	This study‡‡
DUSP22	JSP1, VHX	Act	1wrm	1	—	—	Yokota *et al.* (2007)
DUSP23a	VHZ, LDP-3	Act	2img/4erc	3	—/V	—	Agarwal *et al.* (2008)/Kuznetsov *et al.* (2012)
DUSP23b	PTPMT1	Cont	Mod	3	—	—	This study‡‡
DUSP24	DUSP26	—	—	—	—	—	—
DUSP25	DUSP23a	—	—	—	—	—	—
DUSP26	LDP-4, SKRP3	Cont	4b04/2e0t/4hrf	3	—/—/—	Dimer	Won *et al.* (2013)‡‡/Lokareddy *et al.* (2013)
DUSP27	DUPD1	—	2y96	1	S	Dimer	Lountos *et al.* (2011)
DUSP28	VHP	—	Mod	1	—	—	This study‡‡

† MKB, MKB-containing MKP; Act, A-DUSP with MKP activity; Cont, controversial MKP activity. ‡ Mod, modelled structure; Exp, experimental structure. § Active-site conformation. ¶ S, sulfate; Cl, chloride; P, phosphate; A, acetate; V, vanadate. †† Potential oligomeric states including observation in crystals or homology models. ‡‡ Structures determined in our laboratories.

A-DUSPs lack an MKB, many are able to dephosphorylate MAPKs (Patterson *et al.*, 2009). The MKP and A-DUSP members, which are the focus of this study, are named using numbers after the family name DUSP. MKPs and a subgroup of A-DUSPs with MKP activity have been grouped as MKP-DUSPs (Nunes-Xavier *et al.*, 2011). Other dual-specificity phosphatases are related to the proteins named DUSP. These include phosphatases of regenerating liver (PRLs), cell division cycle 14 proteins (CDC14s), phosphatase and tensin homologues deleted on chromosome 10 (PTENs) and myotubularins (Patterson *et al.*, 2009). These enzymes target substrates other than MAPKs.

DUSPs have diverse roles in development, organogenesis and the immune response. DUSP1 and DUSP9 knockout mice exhibit decreased superior cervical ganglion neurons (Kristiansen *et al.*, 2010) and abnormal placental development (Christie *et al.*, 2005), respectively. DUSP6 is required for proper axial patterning in the zebrafish embryo (Tsang *et al.*, 2004), while DUSP14 appears to regulate co-stimulatory signalling in T cells (Marti *et al.*, 2001). DUSP26 is involved in brain stress signalling (Takagaki *et al.*, 2007). Many DUSPs have been implicated in cancer development; DUSP1 and DUSP4 are increased in breast cancer (Chen *et al.*, 2011; Wang *et al.*, 2003), while DUSP6 is hypermethylated in pancreatic cancer, indicating its role as a tumour suppressor (Xu *et al.*, 2005). DUSP9 also acts as a tumour suppressor (Liu *et al.*, 2007), and expression of DUSP2 and DUSP7 is enhanced in ovarian cancer and myeloid leukaemia, respectively (Givant-Horwitz *et al.*, 2004; Levy-Nissenbaum *et al.*, 2003). DUSP26 has been shown to be amplified in anaplastic thyroid cancers (ATCs; Yu *et al.*, 2007).

The active site of PTPs contains a conserved loop with an HCX_5R motif referred to as the PTP loop or the P-loop (Andersen *et al.*, 2001). In addition to the P-loop, an adjacent loop known as the WPD (Trp-Pro-Asp) loop contains an aspartate residue that functions as a phosphodiester bond-cleaving nucleophile. DUSP3 was the first DUSP for which the three-dimensional structure was determined (Yuvaniyama *et al.*, 1996). The structure includes a central β-sheet surrounded by α-helices, which is similar to that of the classical PTP PTP1B. However, the active-site pocket of DUSP3 is shallower than that of PTP1B, explaining the mechanism by which both serine/threonine and tyrosine are accommodated. The WPD loop of PTP1B is shortened in DUSP3 to become a loop named the D-loop, which lacks the tryptophan and proline of the WPD loop. Despite the handicap of the shallow active-site pocket, there has been significant progress in the development of DUSP inhibitors that can modulate DUSP functions in diseases (Nunes-Xavier *et al.*, 2011). The activities of DUSPs are regulated by specific protein–protein interactions with the MKB (Boutros *et al.*, 2008) and by the cellular redox status (Kamata *et al.*, 2005). A-DUSPs, which lack MKBs, are likely

to interact with other regulatory proteins, which are largely unknown. An analysis of the family-wide structure of the classical phosphatome revealed the classical mechanism of catalytic activity, substrate recognition and regulation of PTPs (Barr *et al.*, 2009). However, there have been no such studies on DUSPs.

To understand the structural and functional characteristics of DUSPs, we carried out family-wide structural studies on DUSPs. There are 26 unique human proteins named DUSPs (DUSP1–DUSP28, including four redundant members; DUSP13 has two submembers 13a and 13b, and DUSP23 has two submembers 23a and 23b; Table 1). Among these 26 DUSPs, we have determined 12 structures, of which nine have been reported previously and three are presented here (Table 1). These newly determined structures (DUSP8, DUSP11 and DUSP12) have low sequence similarity (10–40% identities) to previously determined structures. Together with the structures reported by other groups, a total of 19 structures have been experimentally determined. The remaining seven members have high sequence similarity (more than 50% identity) to members whose structures have been experimentally determined, and we were able to construct reliable homology models of these proteins. The family-wide structural library of human DUSPs allows comprehensive analysis of the structural and functional characteristics of this enzyme family, and provides insight into the mechanism of a subfamily-dependent structural switch, substrate/inhibitor specificities and functional regulation. Family-wide characterization of human DUSP structures also provides a framework for the development of therapeutics for cancers and other phosphorylation-related diseases.

2. Materials and methods

2.1. Protein expression and crystallization

The genes for human DUSP8, DUSP11 and DUSP12 were cloned from a brain cDNA library (Clontech, Mountain View, California, USA). Catalytic domains of DUSP8 (residues 160–312, C246S), DUSP11 (residues 27–210, C152S) and DUSP12 (residues 27–191, C97A and C115S) were expressed in *Escherichia coli* BL21 (DE3) cells using the pET-28a expression vector (Novagen, Madison, Wisconsin, USA). For all three DUSPs, cysteine mutations were necessary to obtain diffraction-quality crystals, possibly because the cysteine residues are susceptible to oxidation. DUSP8-, DUSP11- or DUSP12-containing vector-transformed *E. coli* cells were induced with 0.1 m*M* isopropyl β-D-1-thiogalactopyranoside at 18°C overnight. The cells were harvested and then sonicated in lysis buffer consisting of 50 m*M* Tris–HCl pH 7.5, 500 m*M* NaCl, 1% phenylmethylsulfonyl fluoride (PMSF), 4 m*M* β-mercaptoethanol, 5% glycerol (DUSP8 and DUSP11) or lysis buffer consisting of 50 m*M* Tris–HCl pH 7.5, 500 m*M* NaCl, 1% PMSF, 5% glycerol (DUSP12). His-tagged proteins were then purified by nickel-affinity chromatography and the His tag was removed by cleavage with thrombin.

DUSP8 was further purified by SP-Sepharose, DUSP11 by Q-Sepharose and DUSP12 by Q-Sepharose ion-exchange chromatography. The proteins were further purified by Sephacryl S-100 (DUSP8 and DUSP11) or S-200 (DUSP12) size-exclusion chromatography after dialysis against a buffer consisting of 20 m*M* HEPES–NaOH pH 7.5, 200 m*M* NaCl, 10 m*M* DTT, 5% glycerol (DUSP8), a buffer consisting of 20 m*M* Tris–HCl pH 8.0, 200 m*M* NaCl, 2 m*M* DTT, 5% glycerol (DUSP11) or a buffer consisting of 25 m*M* HEPES pH 7.5, 200 m*M* NaCl, 1 m*M* DTT, 5% glycerol (DUSP12). Dialyzed proteins were concentrated to 12 mg ml^{-1} (DUSP8), 50 mg ml^{-1} (DUSP11) or 35 mg ml^{-1} (DUSP12) for use in crystallization studies.

Crystallization was performed at 18°C using the hanging-drop method. Initial trials were carried out using commercial screening kits including Crystal Screen, Crystal Screen 2 and Index (Hampton Research, Aliso Viejo, California, USA) and Wizard 1–4 (Emerald BioSystems, Bedford, Massachusetts, USA). The highest quality crystals were grown by mixing 1.8 µl (DUSP8 and DUSP11) or 1 µl (DUSP12) protein solution and an equal volume of reservoir solution consisting of 25% PEG 3350, 0.1 *M* bis-tris pH 5.5, 200 m*M* ammonium sulfate (DUSP8), 25% PEG 3350, 0.1 *M* HEPES–NaOH pH 7.5, 200 m*M* ammonium acetate (DUSP11) or 16% PEG 8000, 36 m*M* potassium phosphate monobasic, 20% glycerol (DUSP12). Within one week, all crystals had grown to their maximum size.

2.2. Structure determination

Diffraction data were collected on beamlines 5C and 7A at the Pohang Light Source (PAL, Kyungbuk, Republic of Korea). For data collection, the crystal in the droplet was transferred to a cryoprotective solution consisting of the mother liquor supplemented with 20% glycerol and flash-cooled in a nitrogen-gas stream at −180°C. Data were processed using *HKL*-2000 (Otwinowski & Minor, 1997). Structures were determined by the molecular-replacement method. For the structure determination of human DUSP8, DUSP11 and DUSP12, structures of human DUSP10 (PDB entry 1zzw; Jeong *et al.*, 2006), baculovirus RNA phosphatase (PDB entry 1yn9; Changela *et al.*, 2005) and mouse DUSP28 (PDB entry 2hcm; Almo *et al.*, 2007) were used as search models, respectively. Molecular-replacement searches were performed using *Phaser* (DUSP8 and DUSP11; McCoy *et al.*, 2007) and *PHENIX* (DUSP12; Adams *et al.*, 2010). Initial rigid-body refinement of the molecular-replacement solution yielded $R_{\rm cryst}$ values of 55.2, 53.0 and 38.6% for DUSP8, DUSP11 and DUSP12, respectively. 5% (DUSP8 and DUSP11) or 10% (DUSP12) of the data were left aside for the calculation of $R_{\rm free}$ values. During refinement using *CNS* (Brünger *et al.*, 1998; DUSP8 and DUSP11) and *PHENIX* (DUSP12), extra electron densities appeared near the active sites in all three DUSPs. The final refinement cycles were carried out using *PHENIX* for all three DUSPs. These densities were fitted as sulfate, phosphate or chloride ions (two sulfates for DUSP8, one phosphate and one chloride for DUSP11 and one phosphate for DUSP12). *Coot* (Emsley *et al.*,

Table 2
Data and refinement statistics.

Values in parentheses are for the highest resolution shell.

	DUSP8	DUSP11	DUSP12
Data collection			
Space group	$P4_12_12$	$P6_3$	$P4_12_12$
Unit-cell parameters (Å, °)	$a = b = 65.85$, $c = 124.50$, $\alpha = \beta = \gamma = 90$	$a = b = 94.78$, $c = 44.30$, $\alpha = \beta = 90$, $\gamma = 120$	$a = b = 50.55$, $c = 128.63$, $\alpha = \beta = \gamma = 90$
Resolution (Å)	1.9 (2.00–1.90)	2.4 (2.47–2.40)	2.0 (2.11–2.00)
Reflections (total/unique)	274358/22371	101108/9276	88611/11473
Completenesss (%)	99.9 (99.8)	99.4 (94.0)	96.5 (96.5)
R_{merge}† (%)	6.0 (27.3)	4.5 (30.3)	7.1 (16.1)
$\langle I/\sigma(I)\rangle$	8.0 (2.8)	54.3 (8.4)	6.2 (3.9)
Refinement			
No. of atoms	2522	1540	1331
R_{cryst}/R_{free} (%)	17.6/20.7	17.8/21.9	16.9/21.5
R.m.s. deviations			
Bond distances (Å)	0.008	0.007	0.007
Bond angles (°)	1.12	1.15	1.05
Average B factor (Å^2)	27.8	61.4	34.3

† $R_{merge} = \sum_{hkl}\sum_i |I_i(hkl) - \langle I(hkl)\rangle| / \sum_{hkl}\sum_i I_i(hkl)$, where $I_i(hkl)$ is the intensity of the ith measurement of an equivalent reflection with indices hkl.

2010) was used for model building. We identified water positions in the final phases of refinement.

The final model of DUSP8 at 1.9 Å resolution consisted of residues 160–310 of chain *A*, residues 159–303 of chain *B*, two sulfate ions per chain and 157 water molecules, yielding final R_{cryst} and R_{free} values of 17.6 and 20.7%, respectively. The final model of DUSP11 at 2.4 Å resolution consisted of residues 28–208, one phosphate ion, one chloride ion and 30 water molecules, yielding final R_{cryst} and R_{free} values of 17.8 and 21.9%, respectively. The final model of DUSP12 at 2.0 Å resolution contained residues 27–189 (residues 65–70 lacked electron density and were not included in the model), one phosphate ion and 93 water molecules, yielding final R_{cryst} and R_{free} values of 16.9 and 21.5%, respectively. For all three DUSP structures there were no residues in the disallowed regions of the Ramachandran plot calculated by *MolProbity* (Chen *et al.*, 2010). Table 2 summarizes the data and refinement statistics.

For DUSPs with high sequence identities (greater than 50%) to other DUSPs for which structures were available, three-dimensional structures were constructed using homology modelling. Homology models of the catalytic domains of human DUSP1, DUSP7, DUSP13a, DUSP16, DUSP21, DUSP23b and DUSP28 were built using the structures of human DUSP4, DUSP6, DUSP26, DUSP8 and DUSP18 and mouse DUSP23b and DUSP28, respectively. The sequence identities of each pair are listed in Supplementary Table S1.[1] All homology models except for that of DUSP16 were constructed using the *ESyPred3D* server (Lambert *et al.*, 2002). This server utilizes a new alignment strategy with neural networks and performs the alignments by combining several alignment programs. For homology modelling of DUSP16, the program *MODELLER* (Sali & Blundell, 1993) was used because the target structure (human DUSP8) was not available in the Protein Data Bank (PDB) at the time. A sequence alignment between DUSP16 and DUSP8 was derived with *ClustalW* (Larkin *et al.*, 2007) using the BLOSUM matrices to score the alignments. Based on the best-scoring sequence alignment, the structure of DUSP16 was constructed. For model building, we employed an optimization method involving conjugate gradients and molecular dynamics to minimize violations of spatial restraints.

2.3. Inhibitor-specificity assay

For the PTP enzyme assay, we expressed and purified the catalytic domains of human DUSPs and related enzymes in active forms. Supplementary Table S2 lists the amino-acid regions of DUSPs and related enzymes that yielded stable protein expression in *E. coli*. The expression and purification procedures for the constructs in the table were similar to those used in the crystallization of DUSP8, DUSP11 and DUSP12. Some enzymes required an active-site cysteine-to-serine mutation for stable protein expression. In the inhibitor-specificity assay, we chose representative enzymes that yielded stable protein expression without the active-site mutation.

Inhibitor compounds were purchased from InterBioScreen Ltd (Moscow, Russia). Inhibitors were added to the reaction mixture (to a final inhibitor concentration of 50 µ*M*) before starting the PTP enzyme reaction. The PTP activity assay was performed using 6,8-difluoro-4-methylumbelliferyl phosphate (DIFMUP) as a substrate at room temperature. Purified DUSP catalytic domains were mixed with 10 µ*M* DIFMUP in a buffer consisting of 20 m*M* Tris–HCl pH 8.0, 0.01% Triton X-100, 5 m*M* DTT. The reaction mixtures were immediately placed in a fluorometer (Victor3000, Perkin Elmer, Waltham, Massachusetts, USA) and the fluorescence was measured with excitation and emission wavelengths of 355 and 460 nm, respectively. The percentage inhibition by each inhibitor was estimated by comparing the initial velocities of enzyme reaction with or without the inhibitor. For ideal estimation of the initial velocity of the enzyme reaction, we first selected an appropriate DUSP concentration at which the progression curve of the enzyme reaction exhibited a linear increase from 0 to 15 min and reached saturation before 20 min. A linear increase of the progression curve at a measurable speed was necessary for reliable measurement of initial velocity. Optimal DUSP concentrations are listed in the left-most column of Supplementary Table S3. The initial velocity of each reaction was obtained by measuring the fluorescence increase from 1 to 4 min (30 s intervals) of the corresponding reaction.

2.4. Surface calculation using the Voronoi diagram

To assess the superposition quality between the two protein surfaces in the regions of interest, the *BetaSuperposer* algorithm (Kim & Kim, 2012) based on the beta-complex theory was used. For the superposition of two surfaces within a cutoff radius of R, a set of sample points were computed for each of the surfaces. Next, the two sets of points were superposed so

[1] Supporting information has been deposited in the IUCr electronic archive (Reference: MH5099).

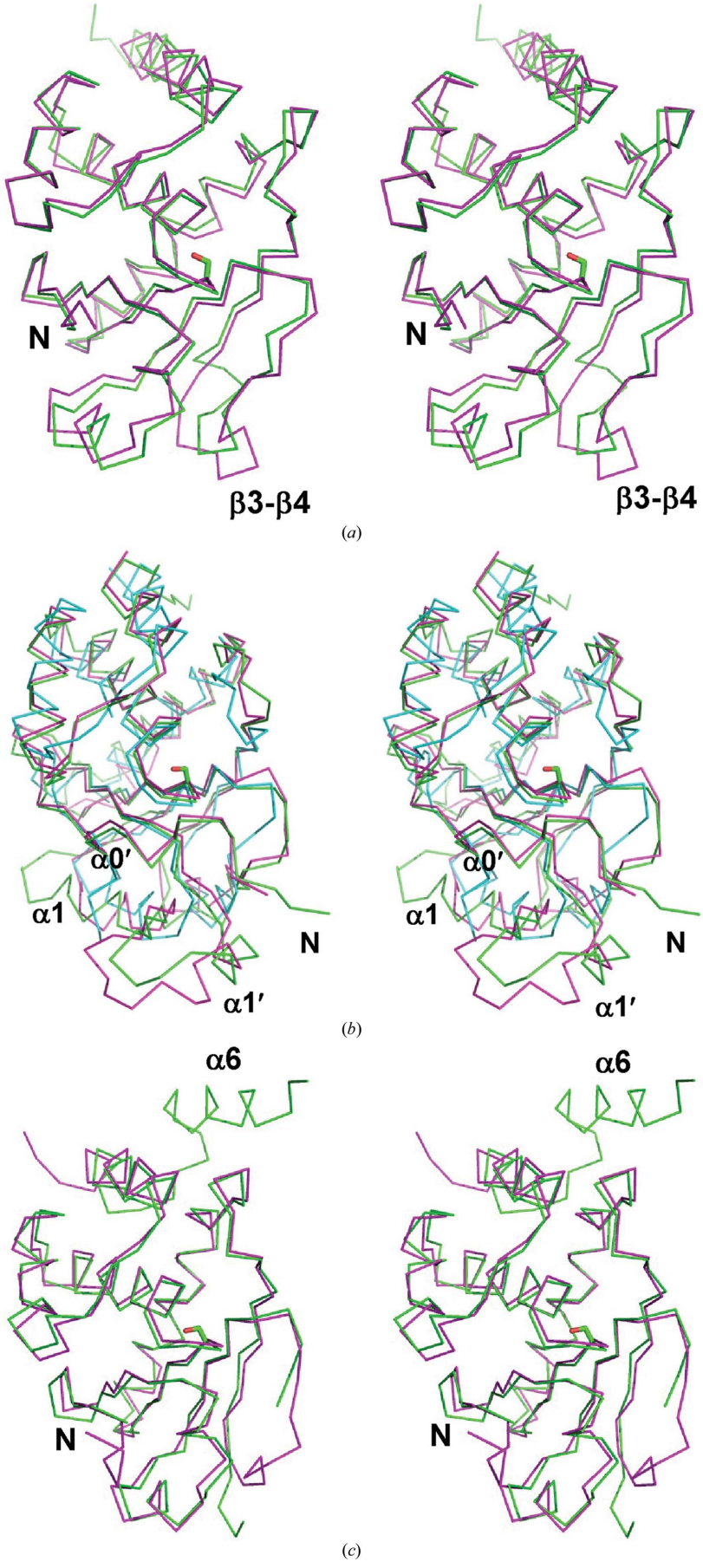

that the sum of the Euclidean distances between the closest pairs of points, where each point is from a different set, was minimized.

2.5. Redox-sensitivity assay

For the oxidation and reduction cycles of DUSPs, we first determined the hydrogen peroxide concentration that completely inhibited enzyme activity. Although some DUSPs lost their enzyme activity at 50–100 μ*M* hydrogen peroxide after 5 min of incubation, several enzymes only lost their enzyme activity at higher hydrogen peroxide concentrations. Thus, we used 200 μ*M* hydrogen peroxide because all DUSPs lost their activities at this concentration. After a 5 min hydrogen peroxide incubation, the oxidized DUSPs were reduced by treatment with 100 m*M* DTT for 20 min and the recovered enzyme activities of the DUSPs were measured. The PTP activity assay was performed using the same procedures as used in the inhibitor-specificity assay.

3. Results and discussion

3.1. Novel DUSP structures

We experimentally determined the catalytic domain structures of human DUSP8, DUSP11 and DUSP12, which had low

Figure 1
Overall comparison of the novel DUSP structures. The novel DUSP structures (human DUSP8, DUSP11 and DUSP12) were superposed with related structures. The views of the figures are similar to each other and the active-site cysteine residues (mutated to serine residues in all three of the novel DUSP structures; C246S, C152S and C115S in DUSP8, DUSP11 and DUSP12, respectively) are indicated as a side-chain representation in the centre of the figures. The figures are presented in stereo. (*a*) Superposition of DUSP8 (green) and DUSP10 (magenta). The location of the N-terminus is indicated in the figure. DUSP8 and DUSP10 have their N-termini in similar locations. (*b*) Superposition of DUSP11 (green), DUSP23a (cyan) and baculovirus RNA 5′-phosphatase (magenta). The location of the N-terminus of DUSP11 is indicated in the figure. Baculovirus RNA 5′-phosphatase has its N-terminus in a similar region, whereas that of DUSP23a is located at the left-hand side of the figure as in (*a*) and (*c*). The unique regions of DUSP11 (α0′, α1′ and α1) are indicated in the figure. (*c*) Superposition of DUSP12 (green) and DUSP5 (magenta). The location of the N-terminus is indicated in the figure. Both DUSP12 and DUSP5 have their N-termini in similar locations. The extra C-terminal helix (α6) of DUSP12 is indicated in the figure.

sequence identities to previously determined DUSP structures. DUSP8 is predominantly expressed in the brain and dephosphorylates Jun kinases (JNKs), leading to inactivation of JNK-mediated cell death in brain ischaemia (Huang *et al.*, 2013). DUSP11 is a novel p53-regulated gene product that has a strong dephosphorylation activity towards RNA substrates and may regulate RNA splicing (Caprara *et al.*, 2009). DUSP12 is an oncogene whose overexpression is correlated with increased cell motility and resistance to apoptosis (Cain *et al.*, 2011).

The overall structures of the DUSP8, DUSP11 and DUSP12 catalytic domains show a canonical PTP catalytic domain fold with the central β-sheet surrounded by α-helices on both sides of the β-sheet (Fig. 1). In the crystal of DUSP8, the asymmetric unit contains two molecules of DUSP8. However, the contact between the two molecules is not extensive and DUSP8 exists as a monomer in solution based on the results of size-exclusion chromatography (data not shown). The two molecules in the asymmetric unit are nearly identical except for differences in the N- and C-terminal boundaries (chain *A*, residues 160–310; chain *B*, residues 159–303). We chose chain *A* for structure description. Both DUSP11 and DUSP12 contain one molecule in the asymmetric unit and there are no crystal contacts that are sufficiently extensive for dimer formation. Both DUSP11 and DUSP12 exist as monomers in solution based on the results of size-exclusion chromatography (data not shown).

Structural similarity searches with previously determined structures using *DALI* (Holm & Rosenström, 2010) revealed that the structure of DUSP8 was most similar to those of slingshot phosphatase 2 (PDB entry 2nt2, *Z*-score 26.4; Jung *et al.*, 2007), DUSP10 (PDB entry 1zzw, *Z*-score 25.4; Jeong, Yoon *et al.*, 2006) and DUSP4 (PDB entry 3ezz, *Z*-score 25.2; Jeong *et al.*, 2009), the structure of DUSP11 was similar to those of baculovirus RNA 5′-phosphatase (PDB entry 1yn9, *Z*-score 26.1; Changela *et al.*, 2005), mouse mRNA-capping enzyme (PDB entry 1i9t, *Z*-score 24.0; Changela *et al.*, 2001), PRL-1 (PDB entry 1xm2, *Z*-score 18.0; Jeong *et al.*, 2005) and DUSP23a (PDB entry 2img, *Z*-score 15.9; Agarwal *et al.*, 2008), and the structure of DUSP12 was similar to those of DUSP5 (PDB entry 2g6z, *Z*-score 23.0; Jeong *et al.*, 2007), slingshot phosphatase 2 (PDB entry 2nt2, *Z* score 23.0) and DUSP4 (PDB entry 3ezz, *Z*-score 22.4).

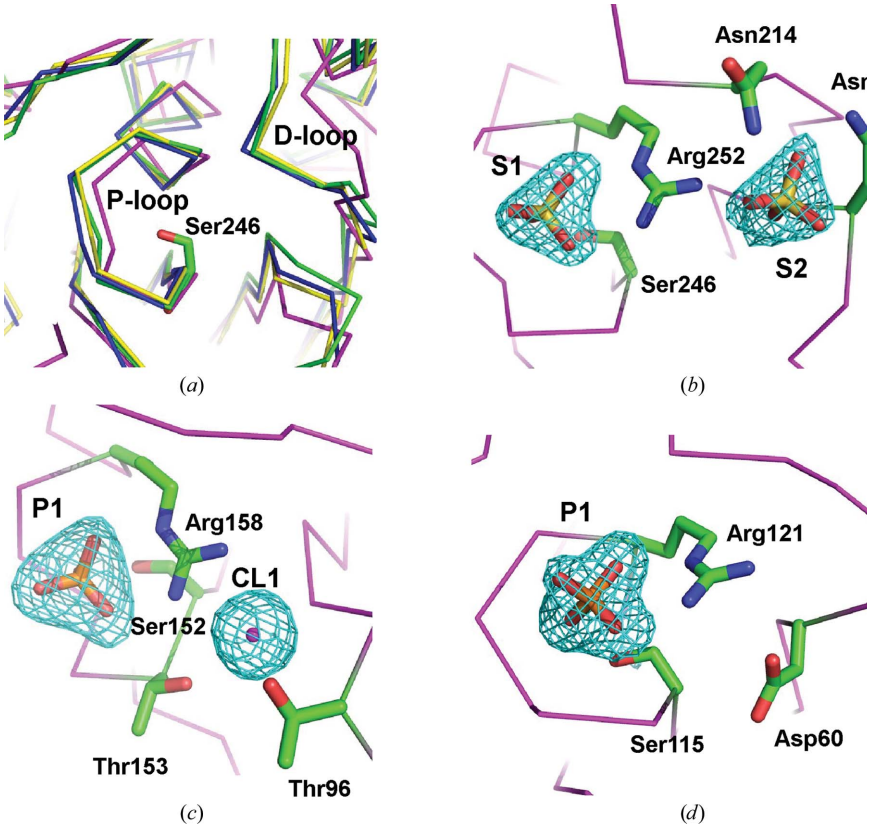

Figure 2
The active sites of the novel DUSP structures. The active-site regions of the novel DUSP structures (human DUSP8, DUSP11 and DUSP12) are presented with bound ions. The views in the figures are similar to each other. In (*b*) and (*c*) the OMIT maps for the bound ions are superposed on the refined DUSP structures. (*a*) The active-site regions of DUSP8 (green), DUSP11 (magenta) and DUSP12 (blue) are superposed together with that of DUSP5 (yellow) as a standard DUSP with the canonical active-site conformation (the closed state). The locations of the P-loops and D-loops are indicated in the figure. The side chain of the active-site cysteine of DUSP8 (mutated to serine) is also shown. (*b*) Active-site residues and ions in DUSP8. Two sulfate ions (S1 and S2) and the side chains of residues near the ions are shown in the figure. (*c*) Active-site residues and ions in DUSP11. Two ions, one phosphate (P1) and one chloride (CL1), and the side chains of the residues near the ions are shown in the figure. (*d*) Active-site residues and an ion in DUSP12. One phosphate ion (P1) and the side chains of residues near the ion are shown in the figure.

Fig. 1 shows comparisons of the overall structures of the newly determined DUSP structures with DUSP structures with high *Z*-scores in the *DALI* search. DUSP8, DUSP11 and DUSP12 were compared with DUSPs10, DUSP23a and DUSP5, respectively. In addition, DUSP11 was also compared with baculovirus RNA 5′-phosphatase (BVP; PDB entry 1yn9), which showed the highest *Z*-value in the *DALI* search. DUSP8 showed good superposition with DUSP10 except for part of loop $\beta3$–$\beta4$ (see below for secondary-structure nomenclature), and the core root-mean-square (r.m.s.) value of the *Coot–SSM* superposition (Emsley *et al.*, 2010) was 1.03 Å for 140 aligned residues out of a total of 151 and 147 residues in DUSP8 and DUSP10, respectively (Fig. 1*a*). In comparison, superposition of DUSP11 and DUSP23a revealed highly variable regions of DUSP11 in the N-terminus and the $\alpha1'$ and $\alpha1$ regions (Fig. 1*b*). The N-terminus of DUSP11 possesses an extended loop structure containing a short α-helix that changes the location of the N-terminus to the opposite side to that of other DUSPs, including DUSP5, DUSP8, DUSP10, DUSP12 and DUSP23a. The $\alpha1'$ and $\alpha1$ regions of

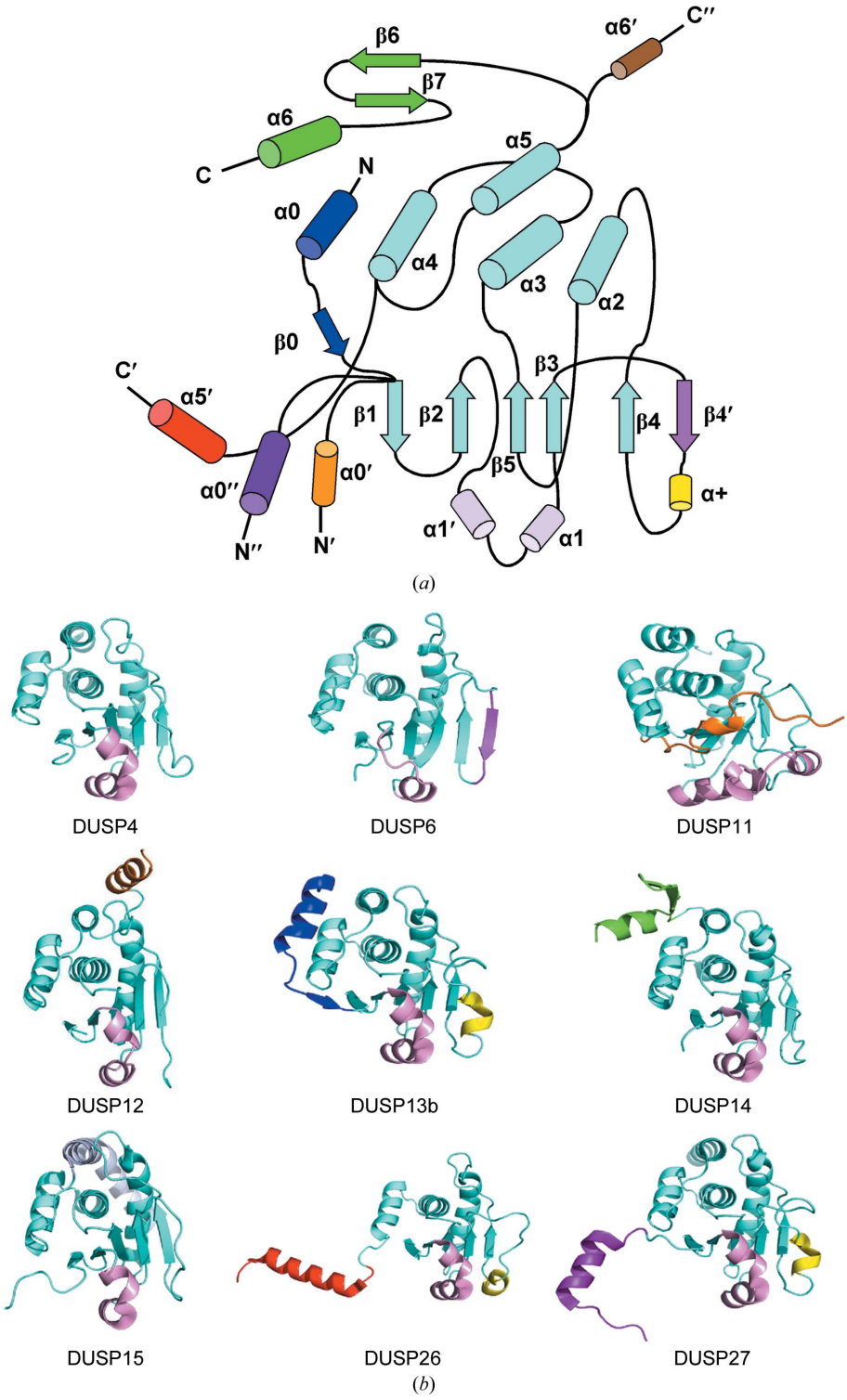

Figure 3
Family-wide structure comparison. (*a*) Schematic representation of secondary-structural elements. The secondary-structural elements of all human DUSPs are displayed in one schematic diagram. The core region (cyan) is conserved in all DUSPs. The structural elements displayed in different colours are those with variations in different DUSP members. (*b*) Examples showing structural differences among human DUSPs. The colour scheme is the same as in (*a*). DUSP4, $\alpha1'$ and $\alpha1$ in pink; DUSP6, $\alpha1$ in pink and $\beta4'$ in magenta; DUSP11, the N-terminal extension including $\alpha0'$ in gold and $\alpha1'$, $\alpha1$ and extended loops in pink; DUSP12, $\alpha1'$ and $\alpha1$ in pink and the C-terminal $\alpha6'$ helix in brown; DUSP13b, $\alpha0$ and $\beta0$ in blue, $\alpha1'$ and $\alpha1$ in pink and $\alpha+$ in yellow; DUSP14, $\alpha1'$ and $\alpha1$ in pink and $\beta6$, $\beta7$ and $\alpha6$ in green; DUSP15, $\alpha1'$ and $\alpha1$ in pink and the extended $\alpha5$ in grey; DUSP26, $\alpha1'$ and $\alpha1$ in pink, $\alpha+$ in yellow and $\alpha5'$ in red; DUSP27, $\alpha0''$ in purple, $\alpha1'$ and $\alpha1$ in pink and $\alpha+$ in yellow.

DUSP11 are much more extended compared with that of DUSP23a. Interestingly, the unique features of DUSP11 are also found in the structure of BVP, indicating evolutionary and functional relationships between these two proteins. In the superposition between DUSP12 and DUSP5, helix $\alpha6$ appears as a unique structure in DUSP12 (Fig. 1*c*). This helix does not exist in other DUSPs (see below). The $\alpha6$ helix of DUSP12 may be involved in the folding of the C-terminal domain of the full-length DUSP12, which mediates its zinc-binding and oxidative stress-recognition functions (Kozarova *et al.*, 2011; Bonham & Vacratsis, 2009).

The superposition of the active-site structures revealed that the P-loops and D-loops of DUSP8 and DUSP12 are well aligned with those of DUSP5, whose active site has a canonical DUSP structure with constitutive enzyme activity (Fig. 2*a*). In comparison, the P-loops and D-loops of DUSP11 are displaced from those of DUSP5, DUSP8 and DUSP12. In particular, the D-loop is completely out of alignment. The D-loop of DUSP11 (residues 90–95; VGHQVP) does not contain the Asp residue that functions as a general acid in most DUSPs. The D-loop of BVP also lacks an Asp, indicating that the RNA dephosphorylation activity of both DUSP11 and BVP does not require an Asp in the D-loop (Changela *et al.*, 2005).

The active-site structure of DUSP8 reveals two sulfate ions bound to the P-loop and the adjacent pocket (Fig. 2*b*). DUSP11 also has two ions (phosphate and chloride) bound to the P-loop and the adjacent pocket, which is a little dislocated from the position of the pocket in DUSP8 (Fig. 2*c*). The DUSP12 active site contains one phosphate ion in the P-loop (Fig. 2*d*). The dual ion-binding sites in DUSP8 are likely to bind two phosphate groups in dually phosphorylated MAP-kinase substrates such as JNK. To test the potential of the DUSP8 ion-binding sites for binding dually phosphorylated MAP-kinase substrates, we carried out a modelling study using DUSP8 and a dually phosphorylated peptide (pT-*X*-pY). The modelling showed that the two

ion-binding pockets could accommodate the two phosphate groups of a dually phosphorylated peptide (data not shown). In comparison, the two ion-binding sites of DUSP11 could not accommodate two consecutive phosphates of triphosphate or diphosphate substrates before the phosphatase reaction. However, the chloride site of DUSP11 is equivalent to the second phosphate site of BVP (Changela *et al.*, 2005) that is likely to bind the phosphate of the leaving group (the β-phosphate of ADP formed from ATP or the α-phosphate of AMP formed from ADP) after the cleavage of the phosphoanhydride bond. Thus, the two ion-binding sites of DUSP11 may be used in a substrate/product-binding mechanism similar to that of BVP for dually or triply phosphorylated RNA substrates.

3.2. Structural classification

The structural superposition of all human DUSPs exhibits good alignment in the core region, but there are deviations in the loops and secondary structures outside the core. A schematic structural comparison of all human DUSPs is presented in Fig. 3 and Supplementary Table S4. Variations in DUSP structures are found in the middle of the domain (mid-domain) as well as at the N- and C-termini (Fig. 3*a*). The mid-domain variations include helices $\alpha1'$ and $\alpha1$ between β-strands $\beta2$ and $\beta3$. Other mid-domain variations are strand $\beta4'$ and helix $\alpha+$, which are formed by a structural switch of strand $\beta4$ and flanking loops. The N- and C-terminal variations may arise from either the artificial truncation of regions outside the catalytic domain or from physiological differences. To show the two possibilities, we list full-length amino-acid ranges together with the regions of expression and structural analysis in Supplementary Table S2. The table shows that there are various DUSP structures with full or near full-length sequences. In these cases, the terminal variations represent physiological structures. For example, DUSP14 and DUSP18, which are of near full length in their C-termini, have the C-terminal extension $\beta6/\beta7/\alpha6$ (Supplementary Tables S2 and S4). This $\beta6/\beta7/\alpha6$ extension is not observed in other full-length DUSPs including DUSP2, DUSP3, DUSP13b, DUSP23a and DUSP26. C-terminal domain swapping in the full-length DUSP26 ($\alpha5'$) also appears to originate from physiological differences in the full-length proteins (Supplementary Tables S2 and S4). Fig. 3(*b*) presents characteristic mid-domain and/or terminal variations of representative DUSP structures.

The secondary-structural characteristics of individual DUSPs show a correlation with the sequence-based phylogenetic tree that divides the 26 DUSPs into five groups (G1–G5; Fig. 4). Structural considerations further divide the G1 group into two subgroups: G1a and G1b. Although the G1a and G1b DUSPs have high sequence homology, one loop near the active site in the G1a DUSPs moves away and forms a characteristic β-strand ($\beta4'$), resulting in significantly different structures of the G1b DUSPs (see below). The G2 DUSPs (four of five members) have an extended/divided $\alpha5$ helix or an extra α-helix ($\alpha6'$). The G3 DUSPs (two of three members) have a $\beta6/\beta7/\alpha6$ extension in the C-terminus. The G4 DUSPs (three of five members) show domain-swapped helices ($\alpha0''$ or $\alpha5'$). The G4 and G5 DUSPs have an $\alpha+$ helix.

3.3. Loop-to-strand conformation switch

The family-wide superposition of DUSP secondary structures reveals that several members undergo conformational switches from a loop near the active site to an extra β-strand in the central β-sheet. These include DUSP2, DUSP6, DUSP7 and DUSP9, which constitute the G1b group. The structural transition is likely to be owing to movement of the D-loop to an outward position (an inactive conformation) that pushes loop $\beta3$–$\beta4$ towards the edge of the central β-sheet to form strand $\beta4'$ (Supplementary Fig. S1). Among the four DUSPs with loop-to-strand switches, three are of Pyst-type DUSPs (DUSP6, DUSP7 and DUSP9), indicating that the switch is more favoured in the Pyst type than other DUSPs. Pyst-type DUSPs are highly specific for extracellular receptor kinase (ERK; Groom *et al.*, 1996; Dickinson *et al.*, 2002). This specificity is thought to originate from the ability of the Pyst-type DUSPs to form a binary complex with ERK, and the

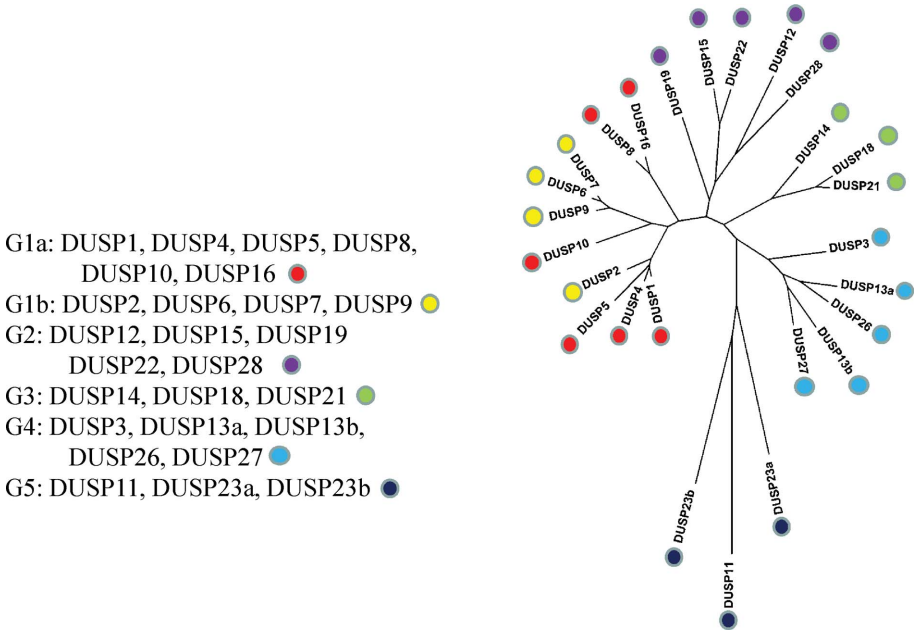

Figure 4
Phylogenetic tree. A phylogenetic tree of human DUSPs was built from catalytic domain sequences. Sequences were aligned using *ClustalW* (Larkin *et al.*, 2007). Phylogenetic trees were inferred using the maximum-likelihood (ML) method and the Poisson correction model using *MEGA* (Tamura *et al.*, 2011). Support for each interior branch was tested with 100 bootstrap replicates. DUSP members in different groups are indicated by differently coloured dots.

loop-to-strand switch is likely to be necessary for complex formation. NMR analysis revealed that strand $\beta4'$ of DUSP2 forms part of the MKB interactions together with helices $\alpha2$ and $\alpha5$ (Farooq *et al.*, 2003). The interaction between MKB and strand $\beta4'$ may lock the catalytic domain in an inactive conformation.

In the DUSPs with the loop-to-strand switch, interaction between the N-terminal MKB domain and substrate may trigger a conformational change in the catalytic domain towards an active conformation (Stewart *et al.*, 1999). Consistent with this hypothesis, the presence of ERK in cells significantly increased the phosphatase activity of cellular DUSP6 (Camps *et al.*, 1998). The *in vitro* catalytic activity of DUSP6 is low in the absence of ERK, indicating that small-molecule substrate binding alone cannot induce a conformational change. Binding of ERK to the MKB domain is likely to provide more interactions and to facilitate the conformational change of the D-loop from the inactive state to the closed and active state for optimal phosphatase activity (Fjeld *et al.*, 2000; Zhou *et al.*, 2006).

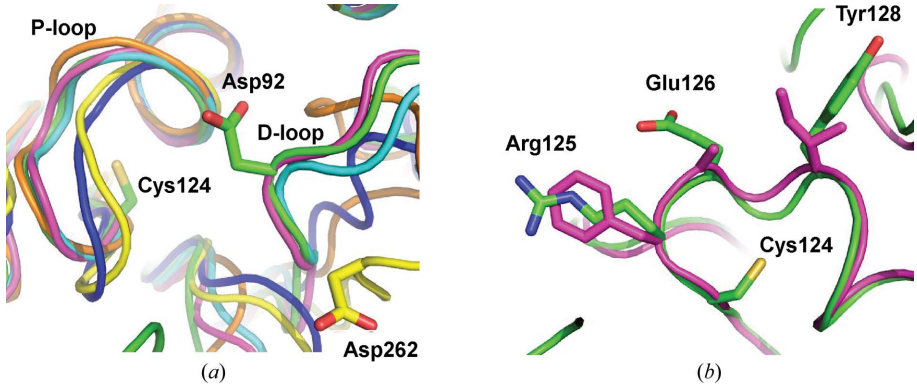

Figure 5
Conformation of the active-site region. (*a*) Comparison of the active-site loops. The structures of the ASC1 members DUSP3, DUSP10 and DUSP15, the ASC2 members DUSP6 and DUSP9 and the ASC3 member DUSP23a are superposed. Colour codes are green, cyan, pink, yellow, blue and gold for DUSP3, DUSP10, DUSP15, DUSP6, DUSP9 and DUSP23a, respectively. The side chains of Cys124 of DUSP3, Asp92 of DUSP3 and Asp262 of DUSP6 are presented in the figure. (*b*) Different environments of the active sites. Representative side chains of P-loop residues in the superposed structures of DUSP3 and DUSP15 are presented. Arg125, Glu126 and Tyr128 of DUSP3 (green) correspond to Phe89, Ala90 and Ile92 of DUSP15 (magenta), respectively. The P-loop residues of DUSP3 (Cys124, Arg125, Glu126 and Tyr128) are labelled in the figure.

When DUSPs with no loop-to-strand switches are superimposed, most secondary structures show good alignment among DUSPs. However, loop $\beta3$–$\beta4$ shows characteristic variations (Supplementary Fig. S1). Currently, it is not clear what functions the loop region mediates. One possibility is that the loop is involved in substrate or regulatory protein interactions. Diverse loop conformations may be beneficial for increasing the specificities towards target proteins. In MKB-containing MKPs, the loop region may be involved in interactions with MKB, as shown in the DUSP2 structure (Farooq *et al.*, 2003). The variation also indicates that this region may be flexible and that the loop-to-strand switch may occur in DUSPs that do not contain the switch. Switching may be induced by the binding of regulatory proteins.

3.4. Active-site loop diversity

Most DUSPs contain the D-loop in the closed state (active-site conformation 1; ASC1 in Table 1). This is in contrast to the classical PTPs, which have an open state in more than half of the structures (Barr *et al.*, 2009). Among the 26 human DUSPs, only DUSP2, DUSP6, DUSP7, DUSP9, DUSP11, DUSP13a, DUSP23a, DUSP23b and DUSP26 are in an open state (Table 1). The first four of these (DUSP2, DUSP6, DUSP7 and DUSP9) have characteristic loop-to-strand switches (ASC2), while the others (DUSP11, DUSP13a, DUSP23a, DUSP23b and DUSP26) are in an open state without the loop-to-strand switch (ASC3). Three of the four ASC2 members (DUSP6, DUSP7 and DUSP9) are Pyst-type DUSPs (Table 1) and three of the five ASC3 members (DUSP11, DUSP23a and DUSP23b) are G5 members, indicating a correlation between active-site conformation and sequence/structure group.

Fig. 5(*a*) compares representative members of the ASC1, ASC2 and ASC3 groups. The ASC1 members (DUSP3, DUSP10 and DUSP15) have the canonical P-loop conformation and the closed D-loop conformation. In the closed D-loop conformation, the aspartate residue functioning as a general acid presents its side chain towards the active-site pocket. The ASC2 members (DUSP6 and DUSP9) exhibit the open D-loop conformation. The aspartate residue in the D-loop of the ASC2 members is located away from the active-site pocket. The P-loops of the ASC2 members are also displaced from the canonical P-loop conformation. The ASC3 member (DUSP23a) has the P-loop in a slightly deformed conformation and the D-loop in a completely deformed state.

Despite the conservation of the P-loop main chain in most DUSPs, including the 17 ASC1 members, there are variations in the side chains. For example, alignment of the P-loops of two ASC1 members, DUSP3 and DUSP15, shows that the main-chain conformations match each other well, whereas the side-chain conformations differ except for the catalytic cysteine (Fig. 5*b*). Tyr128, Glu126 and Arg125 of DUSP3 are replaced by Ile92, Ala90 and Phe89 in DUSP15, respectively. The structural differences caused by these replacements are likely to result in different specificities for substrates and can be exploited in the development of inhibitors.

The structures of many of the DUSPs show ions bound to the active-site pocket (Table 1), including sulfate, chloride, phosphate and acetate. The ions contribute to the stability of the P-loop conformation through interactions with the amide groups of the loop. There are also interactions with the D-loop, indicating that the ions may stabilize the D-loop conformation in a closed state. However, ion binding does not appear to be sufficient to induce a closed state in DUSPs

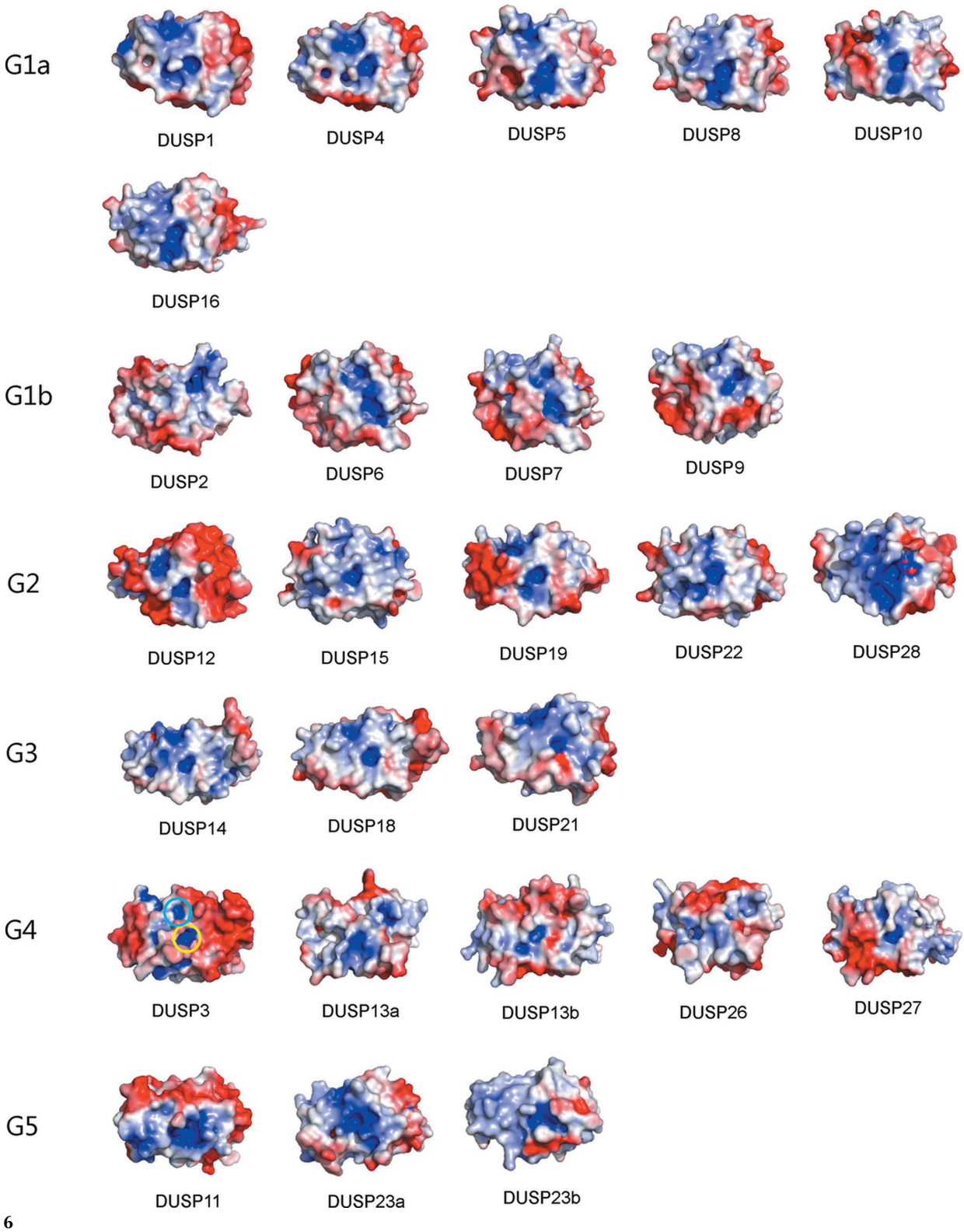

Figure 6
Molecular surfaces of DUSP structures. Molecular surfaces of 26 human DUSP structures were created using *PyMOL* with the *APBS* plugin. Solvent-accessible surfaces produced with structurally aligned DUSPs are coloured by electrostatic potential. Red and blue represent negative and positive potential, respectively. The contour levels for the low, middle and high potentials are −2, 1 and 7, respectively. All surfaces are presented in an equivalent orientation with the active-site pocket in the centre of the figure. The active-site and the secondary phosphate-binding pockets of DUSP3 (G4) are represented as yellow and cyan circles, respectively. To generate the DUSP3 surface, the DUSP3 coordinates from the structure of the DUSP3–p38 peptide complex (PDB entry 1j4x; Schumacher *et al.*, 2002) were used. The contour levels of the DUSP3 surface were adjusted to −2, 2 and 4 to show the secondary phosphate-binding pocket clearly. Some DUSPs form multimers. DUSP13a (model based on DUSP26), DUSP26 and DUSP27 form domain-swapped dimers. DUSP4 and DUSP5 form a 24-mer and a dimer, respectively (for references, see Table 1). In the figure, only the monomeric parts are shown for DUSPs with multimeric states.

because the open-state structures of DUSP6 and DUSP9 also contain a chloride ion and a phosphate ion in the active-site pocket, respectively.

3.5. Surface properties and substrate recognition

The electrostatic surfaces of DUSPs reveal that each DUSP has a unique surface feature (Fig. 6). The positively charged active-site pocket located in the centre of the electrostatic surface is surrounded by neutral regions and negatively charged regions. One characteristic feature common to many DUSPs is the existence of another positively charged pocket near the active-site pocket. This feature is more pronounced in members of the G1a group that are MKB-containing MKPs. MKPs target the bisphosphorylated MAPK substrates with the consensus sequence pT-*X*-pY. The dual positively charged pockets in the G1a DUSPs are necessary for recognizing such substrates.

In DUSP1 and DUSP4, the additional pocket is located above the active-site pocket, whereas the extra pocket of other G1a DUSPs (DUSP5, DUSP8, DUSP10 and DUSP16) is on the opposite side, indicating that the orientation of the substrate peptides may differ in different DUSPs. Previously, the structure of DUSP3 in complex with a bisphosphorylated peptide of the MAPK p38 showed that the extended substrate peptide interacts with a surface groove near the active site (Schumacher *et al.*, 2002). In the structure of the DUSP3–p38 peptide complex, a secondary phosphate-binding site was also identified. The site forms a positively charged pocket involving the side chain of Arg158 (the cyan circle on the DUSP3 surface in Fig. 6).

Similarly to DUSP3, which is not an MKB-containing MKP, some of the A-DUSPs show dephosphorylating activity towards MAPKs. These include DUSP14, DUSP15, DUSP18, DUSP19, DUSP22 and DUSP23a in addition to DUSP3 (Table 1). DUSP21, DUSP23b and DUSP26 exhibit controversial MAPK-dephosphorylating activity. Most of these DUSPs possess the extra positively charged pocket, consistent with their MAPK-dephosphorylating activities. Among the 26 surface structures presented in Fig. 6, seven (DUSP1, DUSP7, DUSP13a, DUSP16, DUSP21, DUSP23b and DUSP28) are homology-modelled structures. Although accurate structural information cannot be deduced from the modelled structures, the surface properties of the modelled structures seem to have implications for substrate or ion binding. For example, the surface of DUSP16 (a homology model based on the DUSP8 structure), which is an MKP, shows a prominent positively charged pocket near the active-site pocket which is equivalent to the second ion-binding site in DUSP8 (the positively charged pocket below the central active-site pocket in Fig. 6). Thus, the extra pocket of DUSP16 may bind a negatively charged ion, as in DUSP8. The G1b members also dephosphorylate bisphosphorylated substrates. However, their surfaces do not show dual positively charged pockets, indicating that the loop-to-strand transition in the active site of the G1b group changes the surface.

In addition to protein substrates such as MAPKs, DUSP substrates include lipids such as phosphatidylglycerol phosphate and phosphatidylinositol 5-phosphate (PtdIns5P; Xiao *et al.*, 2011). The structure of mouse DUSP23b in complex with PtdIns5P revealed that the phosphorylated sugar moiety of PtdIns5P was involved in interactions with the positively charged active-site pocket (Xiao *et al.*, 2011). The active-site surface of DUSP23b (G5 group) is wider than that of the DUSPs in other groups, consistent with the interaction of the active site with the bulky sugar group in PtdIns5P (Fig. 6). This wide active-site surface property is shared with the other G5 DUSPs DUSP11 and DUSP23a. DUSP11 has phosphatase activity towards RNA 5′-triphosphates and diphosphates, which have bulky sugar moieties, consistent with the wide active-site surface (Deshpande *et al.*, 1999).

The regions flanking the catalytic domain of DUSPs also play important roles in substrate recognition of DUSPs. There are ten DUSPs that contain the MKB in the N-terminus of the catalytic domain (Table 1). The differential affinity of MKBs towards particular MAPK substrates determines the substrate specificity of the DUSP catalytic domain (Tanoue *et al.*, 2002). The structure of the complex between the MKB of DUSP10 (MKP-5) and p38 kinase revealed that two helices (α2 and α3) of DUSP10 MKB make specific interactions with p38 kinase (Zhang *et al.*, 2011). The zinc-binding C-terminal flanking region of DUSP12 is involved in cell-cycle modulation and redox-regulation activity (Kozarova *et al.*, 2011; Bonham & Vacratsis, 2009). Thus, the structures of full-length DUSPs are necessary for a complete understanding of the function and specificity of DUSPs.

3.6. Inhibitor-specificity profiling

DUSPs can bind various compounds that inhibit phosphatase activity (Nunes-Xavier *et al.*, 2011). These inhibitors have the potential to be used as therapeutics for cancer, inflammation and neurological disorders. In developing such compounds as therapeutics, the specific inhibition of a given DUSP is crucial. Previously, we carried out virtual screening studies based on the structures of DUSPs and identified various compounds (Park *et al.*, 2008*a*,*b*, 2011; Supplementary Fig. S2). The compounds inhibited DUSP phosphatase activity with an IC_{50} ranging from 2 to 10 μM. However, the enzyme specificity of the compounds has not been analyzed.

We analyzed the specificity of these compounds for human DUSPs and related enzymes [PRLs, slingshot phosphatases (SSHs) and RNGTT; Supplementary Table S3 and Fig. S3]. We produced DUSPs and related enzymes using the optimal constructs for the expression and purification of the catalytic domains (§2 and Supplementary Table S2). Among the ten different compounds tested, six (compounds 1, 3, 4, 7, 9 and 10) showed more than 50% inhibition of DUSP3, DUSP5, DUSP15 and DUSP23a, indicating that there may be common structural features in their active-site pockets. Two compounds, 1 and 3, showed highly potent inhibition of most DUSPs tested. Compared with inhibitors showing common inhibition of several DUSPs, some inhibitors were specific

to one or two DUSPs. For example, compound 6 potently inhibited only DUSP3 (89.7%), whereas the same compound had low inhibitory activities towards DUSP12 (10.2%), SSH2 (3.7%) and RNGTT (7.5%).

The molecular geometries of DUSPs in the active-site pocket were compared using a program employing the Voronoi algorithm (Kim & Kim, 2012). In this analysis, beta-points within a sphere of cutoff radius 6.0 Å from the active-site cysteine S atom were compared between pairs of DUSP structures. The depth of the active-site pocket in DUSPs is approximately 6.0 Å, rationalizing the choice of cutoff radius. The r.m.s. deviations between the beta-points were used to construct a phylogenetic tree (Supplementary Fig. S4). In the phylogenetic tree, DUSP3, DUSP5, DUSP15 and DUSP23a were close together, consistent with their inhibition-specificity profiles. Supplementary Fig. S5 compares the active-site pockets of DUSPs with similar inhibition profiles (DUSP3 with DUSP15 or DUSP23a) and those with different inhibition profiles (DUSP3 with DUSP13b or DUSP28). The figure shows that the active-site pocket geometry of DUSP3 matches better (more green regions) with DUSP15 or DUSP23a than it does with DUSP13b or DUSP28 (more red regions). The consistency between the active-site pocket geometry and the inhibition specificity indicates that an active-site pocket geometry comparison can be used to predict the inhibition profiles of DUSPs.

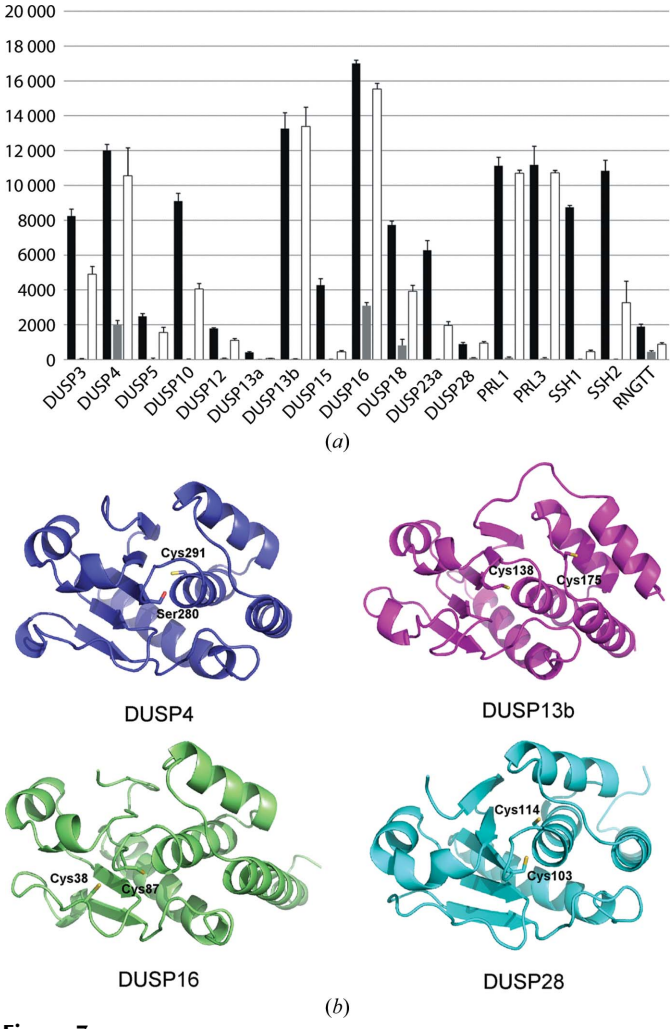

Figure 7
Reversibility of oxidized DUSPs. (*a*) Redox-dependent enzyme activities of human DUSPs. Analysis was carried out with DUSPs and related proteins that could be expressed and purified as active forms (Supplementary Table S2). The *y* axis is an arbitrary fluorescence unit per minute that represents the initial velocity of the enzyme reaction. For each enzyme, three bars are shown for the untreated protein (black), the protein treated with hydrogen peroxide (grey) and the protein treated with excess amounts of DTT after hydrogen peroxide treatment (white). Error bars were calculated using at least three measurements. (*b*) Extra cysteines of human DUSPs. Ribbon diagrams of DUSP4, DUSP13b, DUSP16 and DUSP28 are presented in a view with the active-site cysteine residues [Cys280 (mutated to Ser) of DUSP4, Cys138 of DUSP13b, Cys87 of DUSP16 and Cys103 of DUSP28] in the centre of the molecules. The extra cysteine residues (Cys291 of DUSP4, Cys175 of DUSP13b, Cys38 of DUSP16 and Cys114 of DUSP28) near the active-site cysteine are labelled in the molecules.

DUSP3, DUSP5, DUSP15 and DUSP23a are specific towards ERK and/or p38 kinase (Patterson *et al.*, 2009; Liovic *et al.*, 2008; Schmidt *et al.*, 2012; Wu *et al.*, 2004), whereas none of the four DUSPs efficiently dephosphorylates JNK. In comparison, DUSP13b, which has a low match with DUSP3 in the active-site pocket geometry, only dephosphorylates JNK (Katagiri *et al.*, 2011). Thus, the substrate specificity of DUSPs appears to be correlated with both the inhibition-specificity profile and the active-site pocket geometry. Previously, the MKB domain or the global surface characteristics of the catalytic domain were thought to determine the substrate specificity of DUSPs (Boutros *et al.*, 2008). In comparison, the current results indicate that the local active-site pocket geometry also plays an important role in determining the substrate specificity.

3.7. Redox-regulation mechanism

The active-site cysteine residues of PTPs are sensitive to oxidation by reactive oxygen species (ROS), which play vital roles in cellular signalling and transcription (Tonks, 2005). Oxidation of cysteine residues inhibits the enzyme activity of PTPs and extends the half-lives of phosphorylated states of growth-factor receptors and other targets (Rhee *et al.*, 2003). The initial oxidation of the cysteine sulfhydryl moiety generates a sulfenic acid that can revert to a sulfhydryl when oxidative-stress conditions are no longer present. Under sustained oxidizing conditions, however, the sulfenic acid is further oxidized to a sulfinic or sulfonic acid that cannot revert to the reduced form.

Although the redox regulation of DUSPs is crucial in signal transduction processes involving MAP kinase signalling cascades (Kamata *et al.*, 2005), there have been no detailed reports of the structural mechanism of DUSP redox regulation. To understand the family-wide structural mechanism of DUSP redox regulation, we analyzed the ROS response of DUSPs in the context of the structures (Fig. 7 and Supplementary Table S5). The activities of all DUSPs were abolished by treatment with 200 µ*M* hydrogen peroxide for 5 min. At lower concentrations of hydrogen peroxide (50–100 µ*M*), some of the DUSPs retained their activity. In previous studies,

high concentrations of hydrogen peroxide of the order of 1 m*M* induced cellular signal cascades by inhibiting protein phosphatases (Dröge, 2002). Thus, 200 µ*M* hydrogen peroxide is a physiologically relevant condition. Although all tested DUSPs lost enzyme activity on incubation with 200 µ*M* hydrogen peroxide, the reversibility of the loss of activity was highly diverse among DUSP members. When oxidized DUSPs were treated with 100 m*M* DTT, most of the enzyme activity of DUSP4, DUSP13b, DUSP16, DUSP28, PRL1 and PRL3 was restored (high recovery; Fig. 7*a* and Supplementary Table S5). In comparison, the other DUSPs showed varying profiles (medium or low recovery; Fig. 7*a* and Supplementary Table S5).

To explain the differential redox behaviours of DUSPs, we examined their structures and found that three (DUSP4, DUSP16 and DUSP28) of the four high-recovery DUSPs have an extra cysteine within 10 Å of the active-site cysteine (distance between S atoms), whereas only one (DUSP5) of the eight medium-recovery or low-recovery DUSPs has a nearby cysteine within 10 Å of the active-site cysteine (Fig. 7*b* and Supplementary Table S5). In particular, the high-recovery DUSP16 has an extra cysteine with an inter-sulfur distance of 6.57 Å. The nearby cysteine may be able to form a disulfide bond to the active-site cysteine. In the previously reported crystal structure of PRL1, the inter-sulfur distance between the extra cysteine and the active-site cysteine was approximately 5 Å and disulfide-bond formation between the two cysteine residues was demonstrated by mass spectrometry (Jeong *et al.*, 2005). Disulfide-bond formation may protect the active-site cysteine from over-oxidation.

High-recovery DUSPs with inter-sulfur distances of 8–11 Å (DUSP4, 8.95 Å; DUSP13b, 11.13 Å; DUSP28, 8.90 Å) may form disulfide bonds with appropriate structural modifications in the cysteine-containing regions, as in the redox-switch proteins with distantly located cysteine pairs (Ryu, 2012). The structural flexibility of the cysteine-containing regions is required for disulfide-bond formation between distantly located cysteine residues. When an appropriate disulfide bond is not possible owing to structural constraints, sulfenic acid may be converted to sulfenyl amide, which is relatively stable (Salmeen *et al.*, 2003; van Montfort *et al.*, 2003; Yang *et al.*, 2007). Although we found no evidence of sulfenyl amide in DUSP structures, some of the high-recovery or medium-recovery DUSPs may form sulfenyl amides upon oxidation.

The active-site pocket of DUSP15 (a low-recovery DUSP) contains more hydrophobic residues in the P-loop than that of DUSP3 (a medium-recovery DUSP) (Fig. 5*b*). Tyr128, Glu126 and Arg125 of DUSP3 are replaced by Ile, Ala and Phe, respectively, in DUSP15. Recent structural studies of the complex of a peroxiredoxin with hydrogen peroxide revealed that the correct orientation of hydrogen peroxide is important for the reaction with the active-site cysteine (Nakamura *et al.*, 2010). Hydrophobic residues in DUSP15 surrounding the active-site cysteine may provide a geometrical guide for the optimal orientation of approaching hydrogen peroxide molecules by avoiding unnecessary polar interactions. The higher reactivity with hydrogen peroxide is likely to cause irreversible over-oxidation of DUSP15. Thus, the structural characteristics determining the differential redox responses of DUSPs appear to include the presence of nearby cysteine residues, the tendency to form a sulfenyl amide and the active-pocket surface properties.

4. Conclusion

We constructed a family-wide human DUSP structural library through family-wide structure-determination studies together with homology modelling. Family-wide structural analysis of DUSPs and structure-aided biochemical characterization revealed the substrate-specificity and regulation mechanisms of the enzyme family. The loop-to-strand switch in the active-site region of DUSPs was observed only in the Pyst-type DUSPs and DUSP2. The other 22 DUSP members did not show this switch, indicating that the switch is a subtype-specific process. Pyst-type DUSPs showed a high specificity for ERK by forming a tight enzyme–substrate complex. The loop-to-strand switch is likely to play a role in binary complex formation. Although most DUSPs do not show the switch in the current structures, they may switch under specific conditions because the loop involved is highly variable and likely to be flexible. Interactions with appropriate substrates or regulators may trigger the switch in various DUSPs.

Based on the family-wide structural information, we carried out comprehensive analyses of the enzyme-inhibition profile and redox sensitivity. The subgroup of DUSPs inhibited by a particular group of chemical compounds have similar active-site pocket geometries. This correlation coincides with their substrate-specificity characteristics, indicating a novel role of the active-site pocket geometry in substrate specificity. Comparison of redox-response behaviour revealed a role for extra cysteine residues in the recovery of enzyme activity after an oxidation–reduction cycle. We also identified optimal conditions for the high-level production of all DUSP catalytic domains, which can be used for further drug screening and functional studies. Thus, the current study forms a basis for understanding the diverse functions of DUSPs, impacting the future development of potent therapeutics.

This work was supported by the next generation applied-omics project (NRF-2011-0030027, 0030030), a Hanyang University internal grant, and a KRIBB research initiative grant.

References

Adams, P. D. *et al.* (2010). *Acta Cryst.* D**66**, 213–221.
Agarwal, R., Burley, S. K. & Swaminathan, S. (2008). *J. Biol. Chem.* **283**, 8946–8953.
Almo, S. C. *et al.* (2007). *J. Struct. Funct. Genomics*, **8**, 121–140.
Alonso, A., Burkhalter, S., Sasin, J., Tautz, L., Bogetz, J., Huynh, H., Bremer, M. C., Holsinger, L. J., Godzik, A. & Mustelin, T. (2004). *J. Biol. Chem.* **279**, 35768–35774.
Alonso, A., Sasin, J., Bottini, N., Friedberg, I., Friedberg, I., Osterman, A., Godzik, A., Hunter, T., Dixon, J. & Mustelin, T. (2004). *Cell*, **117**, 699–711.

Andersen, J. N., Mortensen, O. H., Peters, G. H., Drake, P. G., Iversen, L. F., Olsen, O. H., Jansen, P. G., Andersen, H. S., Tonks, N. K. & Møller, N. P. (2001). *Mol. Cell. Biol.* **21**, 7117–7136.

Barr, A. J., Ugochukwu, E., Lee, W. H., King, O. N. F., Filippakopoulos, P., Alfano, I., Savitsky, P., Burgess-Brown, N. A., Müller, S. & Knapp, S. (2009). *Cell*, **136**, 352–363.

Bonham, C. A. & Vacratsis, P. O. (2009). *J. Biol. Chem.* **284**, 22853–22864.

Boutros, T., Chevet, E. & Metrakos, P. (2008). *Pharmacol. Rev.* **60**, 261–310.

Brünger, A. T., Adams, P. D., Clore, G. M., DeLano, W. L., Gros, P., Grosse-Kunstleve, R. W., Jiang, J.-S., Kuszewski, J., Nilges, M., Pannu, N. S., Read, R. J., Rice, L. M., Simonson, T. & Warren, G. L. (1998). *Acta Cryst.* D**54**, 905–921.

Cain, E. L., Braun, S. E. & Beeser, A. (2011). *PLoS One*, **6**, e18677.

Camps, M., Nichols, A., Gillieron, C., Antonsson, B., Muda, M., Chabert, C., Boschert, U. & Arkinstall, S. (1998). *Science*, **280**, 1262–1265.

Caprara, G., Zamponi, R., Melixetian, M. & Helin, K. (2009). *J. Cell. Mol. Med.* **13**, 2158–2170.

Changela, A., Ho, C. K., Martins, A., Shuman, S. & Mondragon, A. (2001). *EMBO J.* **20**, 2575–2586.

Changela, A., Martins, A., Shuman, S. & Mondragón, A. (2005). *J. Biol. Chem.* **280**, 17848–17856.

Chen, C.-C., Hardy, D. B. & Mendelson, C. R. (2011). *J. Biol. Chem.* **286**, 43091–43102.

Chen, V. B., Arendall, W. B., Headd, J. J., Keedy, D. A., Immormino, R. M., Kapral, G. J., Murray, L. W., Richardson, J. S. & Richardson, D. C. (2010). *Acta Cryst.* D**66**, 12–21.

Christie, G. R., Williams, D. J., MacIsaac, F., Dickinson, R. J., Rosewell, I. & Keyse, S. M. (2005). *Mol. Cell. Biol.* **25**, 8323–8333.

Deshpande, T., Takagi, T., Hao, L., Buratowski, S. & Charbonneau, H. (1999). *J. Biol. Chem.* **274**, 16590–16594.

Dickinson, R. J., Williams, D. J., Slack, D. N., Williamson, J., Seternes, O. M. & Keyse, S. M. (2002). *Biochem. J.* **364**, 145–155.

Dröge, W. (2002). *Physiol. Rev.* **82**, 47–95.

Emsley, P., Lohkamp, B., Scott, W. G. & Cowtan, K. (2010). *Acta Cryst.* D**66**, 486–501.

Farooq, A., Plotnikova, O., Chaturvedi, G., Yan, S., Zeng, L., Zhang, Q. & Zhou, M. M. (2003). *Structure*, **11**, 155–164.

Fjeld, C. C., Rice, A. E., Kim, Y., Gee, K. R. & Denu, J. M. (2000). *J. Biol. Chem.* **275**, 6749–6757.

Givant-Horwitz, V., Davidson, B., Goderstad, J. M., Nesland, J. M., Tropé, C. G. & Reich, R. (2004). *Gynecol. Oncol.* **93**, 517–523.

Groom, L. A., Sneddon, A. A., Alessi, D. R., Dowd, S. & Keyse, S. M. (1996). *EMBO J.* **15**, 3621–3632.

Guan, K. L., Broyles, S. S. & Dixon, J. E. (1991). *Nature (London)*, **350**, 359–362.

Holm, L. & Rosenström, P. (2010). *Nucleic Acids Res.* **38**, W545–W549.

Huang, Z., Liu, Y., Zhu, J., Wu, H. & Guo, J. (2013). *Int. J. Neurosci.* **123**, 802–809.

Jeffrey, K. L., Camps, M., Rommel, C. & Mackay, C. R. (2007). *Nature Rev. Drug Discov.* **6**, 391–403.

Jeong, D. G., Cho, Y. H., Yoon, T.-S., Kim, J. H., Ryu, S. E. & Kim, S. J. (2007). *Proteins*, **66**, 253–258.

Jeong, D. G., Cho, Y. H., Yoon, T.-S., Kim, J. H., Son, J. H., Ryu, S. E. & Kim, S. J. (2006). *Acta Cryst.* D**62**, 582–588.

Jeong, D. G., Jung, S.-K., Yoon, T. S., Woo, E.-J., Kim, J. H., Park, B. C., Ryu, S. E. & Kim, S. J. (2009). *Proteins*, **76**, 763–767.

Jeong, D. G., Kim, S. J., Kim, J. H., Son, J. H., Park, M. R., Lim, S. M., Yoon, T.-S. & Ryu, S. E. (2005). *J. Mol. Biol.* **345**, 401–413.

Jeong, D. G., Yoon, T. S., Jung, S.-K., Park, B. C., Park, H., Ryu, S. E. & Kim, S. J. (2011). *Acta Cryst.* D**67**, 25–31.

Jeong, D. G., Yoon, T.-S., Kim, J. H., Shim, M. Y., Jung, S.-K., Son, J. H., Ryu, S. E. & Kim, S. J. (2006). *J. Mol. Biol.* **360**, 946–955.

Jung, S.-K., Jeong, D. G., Yoon, T.-S., Kim, J. H., Ryu, S. E. & Kim, S. J. (2007). *Proteins*, **68**, 408–412.

Kamata, H., Honda, S., Maeda, S., Chang, L., Hirata, H. & Karin, M. (2005). *Cell*, **120**, 649–661.

Katagiri, C., Masuda, K., Nomura, M., Tanoue, K., Fujita, S., Yamashita, Y., Katakura, R., Shiiba, K., Nomura, E., Sato, M., Tanuma, N. & Shima, H. (2011). *Mol. Cell. Biochem.* **352**, 155–162.

Kim, J.-K. & Kim, D.-S. (2012). *J. Biomol. Struct. Dyn.* **30**, 684–700.

Kim, S. J., Jeong, D.-G., Yoon, T.-S., Son, J.-H., Cho, S. K., Ryu, S. E. & Kim, J.-H. (2007). *Proteins*, **66**, 239–245.

Koksal, A. C., Nardozzi, J. D. & Cingolani, G. (2009). *J. Biol. Chem.* **284**, 10129–10137.

Kozarova, A., Hudson, J. W. & Vacratsis, P. O. (2011). *Cell Cycle*, **10**, 1669–1678.

Kristiansen, M., Hughes, R., Patel, P., Jacques, T. S., Clark, A. R. & Ham, J. (2010). *J. Neurosci.* **30**, 10820–10832.

Kuznetsov, V. I., Hengge, A. C. & Johnson, S. J. (2012). *Biochemistry*, **51**, 9869–9879.

Lambert, C., Léonard, N., De Bolle, X. & Depiereux, E. (2002). *Bioinformatics*, **18**, 1250–1256.

Larkin, M. A., Blackshields, G., Brown, N. P., Chenna, R., McGettigan, P. A., McWilliam, H., Valentin, F., Wallace, I. M., Wilm, A., Lopez, R., Thompson, J. D., Gibson, T. J. & Higgins, D. G. (2007). *Bioinformatics*, **23**, 2947–2948.

Levy-Nissenbaum, O., Sagi-Assif, O., Kapon, D., Hantisteanu, S., Burg, T., Raanani, P., Avigdor, A., Ben-Bassat, I. & Witz, I. P. (2003). *Oncogene*, **22**, 7649–7660.

Liovic, M., Lee, B., Tomic-Canic, M., D'Alessandro, M., Bolshakov, V. N. & Lane, E. B. (2008). *Exp. Cell Res.* **314**, 2066–2075.

Liu, Y., Lagowski, J., Sundholm, A., Sundberg, A. & Kulesz-Martin, M. (2007). *Cancer Res.* **67**, 10711–10719.

Lokareddy, R. K., Bhardwaj, A. & Cingolani, G. (2013). *Biochemistry*, **52**, 938–948.

Lountos, G. T., Tropea, J. E., Cherry, S. & Waugh, D. S. (2009). *Acta Cryst.* D**65**, 1013–1020.

Lountos, G. T., Tropea, J. E. & Waugh, D. S. (2011). *Acta Cryst.* D**67**, 471–479.

Marti, F., Krause, A., Post, N. H., Lyddane, C., Dupont, B., Sadelain, M. & King, P. D. (2001). *J. Immunol.* **166**, 197–206.

McCoy, A. J., Grosse-Kunstleve, R. W., Adams, P. D., Winn, M. D., Storoni, L. C. & Read, R. J. (2007). *J. Appl. Cryst.* **40**, 658–674.

Montfort, R. L. van, Congreve, M., Tisi, D., Carr, R. & Jhoti, H. (2003). *Nature (London)*, **423**, 773–777.

Nakamura, T., Kado, Y., Yamaguchi, T., Matsumura, H., Ishikawa, K. & Inoue, T. (2010). *J. Biochem.* **147**, 109–115.

Nunes-Xavier, C., Romá-Mateo, C., Ríos, P., Tárrega, C., Cejudo-Marín, R., Tabernero, L. & Pulido, R. (2011). *Anticancer Agents Med. Chem.* **11**, 109–132.

Otwinowski, Z. & Minor, W. (1997). *Methods Enzymol.* **276**, 307–326.

Park, H., Jeon, J.-Y., Kim, S. Y., Jeong, D. G. & Ryu, S. E. (2011). *J. Comput. Aided Mol. Des.* **25**, 469–475.

Park, H., Jung, S.-K., Jeong, D. G., Ryu, S. E. & Kim, S. J. (2008*a*). *Bioorg. Med. Chem. Lett.* **18**, 2250–2255.

Park, H., Jung, S.-K., Jeong, D. G., Ryu, S. E. & Kim, S. J. (2008*b*). *ChemMedChem*, **3**, 877–880.

Patterson, K. I., Brummer, T., O'Brien, P. M. & Daly, R. J. (2009). *Biochem. J.* **418**, 475–489.

Rhee, S. G., Chang, T.-S., Bae, Y. S., Lee, S.-R. & Kang, S. W. (2003). *J. Am. Soc. Nephrol.* **14**, S211–S215.

Ryu, S. E. (2012). *J. Biochem.* **151**, 579–588.

Sali, A. & Blundell, T. L. (1993). *J. Mol. Biol.* **234**, 779–815.

Salmeen, A., Andersen, J. N., Myers, M. P., Meng, T.-C., Hinks, J. A., Tonks, N. K. & Barford, D. (2003). *Nature (London)*, **423**, 769–773.

Sawyer, T. K., Shakespeare, W. C., Wang, Y., Sundaramoorthi, R., Huang, W. S., Metcalf, C. A. III, Thomas, M., Lawrence, B. M., Rozamus, L., Noehre, J., Zhu, X., Narula, S., Bohacek, R. S., Weigele, M. & Dalgarno, D. C. (2005). *Med. Chem.* **1**, 293–319.

Schmidt, F., van den Eijnden, M., Pescini Gobert, R., Saborio, G. P., Carboni, S., Alliod, C., Pouly, S., Staugaitis, S. M., Dutta, R., Trapp, B. & Hooft van Huijsduijnen, R. (2012). *PLoS One*, **7**, e40457.

Schumacher, M. A., Todd, J. L., Rice, A. E., Tanner, K. G. & Denu, J. M. (2002). *Biochemistry*, **41**, 3009–3017.
Stewart, A. E., Dowd, S., Keyse, S. M. & McDonald, N. Q. (1999). *Nature Struct. Biol.* **6**, 174–181.
Takagaki, K., Shima, H., Tanuma, N., Nomura, M., Satoh, T., Watanabe, M. & Kikuchi, K. (2007). *Mol. Cell. Biochem.* **296**, 177–184.
Tamura, K., Peterson, D., Peterson, N., Stecher, G., Nei, M. & Kumar, S. (2011). *Mol. Biol. Evol.* **28**, 2731–2739.
Tanoue, T., Yamamoto, T. & Nishida, E. (2002). *J. Biol. Chem.* **277**, 22942–22949.
Tao, X. & Tong, L. (2007). *Protein Sci.* **16**, 880–886.
Tonks, N. K. (2005). *Cell*, **121**, 667–670.
Tonks, N. K. (2006). *Nature Rev. Mol. Cell Biol.* **7**, 833–846.
Tsang, M., Maegawa, S., Kiang, A., Habas, R., Weinberg, E. & Dawid, I. B. (2004). *Development*, **131**, 2769–2779.
Wang, H. Y., Cheng, Z. & Malbon, C. C. (2003). *Cancer Lett.* **191**, 229–237.
Wei, C. H., Ryu, S. Y., Jeon, Y. H., Yoon, M. Y., Jeong, D. G., Kim, S. J. & Ryu, S. E. (2011). *Proteins*, **79**, 3242–3246.
Won, E.-Y., Xie, Y., Takemoto, C., Chen, L., Liu, Z.-J., Wang, B.-C., Lee, D., Woo, E.-J., Park, S. G., Shirouzu, M., Yokoyama, S., Kim, S. J. & Chi, S.-W. (2013). *Acta Cryst.* D**69**, 1160–1170.
Wu, Q., Li, Y., Gu, S., Li, N., Zheng, D., Li, D., Zheng, Z., Ji, C., Xie, Y. & Mao, Y. (2004). *Int. J. Biochem. Cell Biol.* **36**, 1542–1553.
Xiao, J., Engel, J. L., Zhang, J., Chen, M. J., Manning, G. & Dixon, J. E. (2011). *Proc. Natl Acad. Sci. USA*, **108**, 11860–11865.
Xu, S., Furukawa, T., Kanai, N., Sunamura, M. & Horii, A. (2005). *J. Hum. Genet.* **50**, 159–167.
Yang, J., Groen, A., Lemeer, S., Jans, A., Slijper, M., Roe, S. M., den Hertog, J. & Barford, D. (2007). *Biochemistry*, **46**, 709–719.
Yokota, T., Nara, Y., Kashima, A., Matsubara, K., Misawa, S., Kato, R. & Sugio, S. (2007). *Proteins*, **66**, 272–278.
Yoon, T.-S., Jeong, D. G., Kim, J. H., Cho, Y. H., Son, J. H., Lee, J. W., Ryu, S. E. & Kim, S. J. (2005). *Proteins*, **61**, 694–697.
Yu, W., Imoto, I., Inoue, J., Onda, M., Emi, M. & Inazawa, J. (2007). *Oncogene*, **26**, 1178–1187.
Yuvaniyama, J., Denu, J. M., Dixon, J. E. & Saper, M. A. (1996). *Science*, **272**, 1328–1331.
Zhang, Y.-Y., Wu, J.-W. & Wang, Z.-X. (2011). *Sci. Signal.* **4**, ra88.
Zhou, B., Zhang, J., Liu, S., Reddy, S., Wang, F. & Zhang, Z.-Y. (2006). *J. Biol. Chem.* **281**, 38834–38844.